JOURNAL OF AIRCRAFT
Vol. 31, No. 6, November–December 1994

Dynamic Analysis of Bearingless Tail Rotor Blades Based on Nonlinear Shell Models

Olivier A. Bauchau* and Wuying Chiang†
Rensselaer Polytechnic Institute, Troy, New York 12180

The unique structural features of helicopter bearingless rotors call for the development of design and modeling methodologies for laminated composite flex-structures. Indeed, the flex-structure should be flexible enough to replace the flap, lead-lag, and feathering bearings, while maintaining high strength and stiffness in the axial direction. Laminated composite materials are a material of choice for such an application. Chordwise deformations, transitional zones between different cross sections and localized compressive stresses are all likely to be present in the flex-structure, rendering the validity of a beam model questionable. In this article a nonlinear anisotropic shallow shell model is developed that accommodates transverse shearing deformations, and arbitrarily large displacements and rotations, but strains are assumed to remain small. The displacement-based shell model has six degrees of freedom at each node and allows for an automatic compatibility of the shell and beam models. the model is validated by comparing its predictions with several benchmark problems. A four-bladed composite bearingless tail rotor system is analyzed in detail using the shell model and compared with the predictions of a beam model. Significant differences are observed between the two models, especially in the torsional behavior.

Introduction

MOST of the helicopters that are in service today employ either an articulated or a teetering rotor.[1,2] In recent years, there has been considerable interest in alternate design with an eye toward mechanical simplicity and increasd reliability and maintainability. The hingeless and bearingless rotor concepts are an outgrowth of such efforts.

In an articulated rotor three bearings are placed near the hub attachment of the blade and provide rigid body motions for the blade in flapping, lead-lag, and feathering. This contrasts with the bearingless rotor[3] where all three bearings are replaced by a single flex-structure that provides the required flapping, lead-lag, and pitching flexibility. The design specifications of this flex-structure are unique: on the one hand, the flex-structure must be strong enough to carry the large centrifugal forces and bending moments, and on the other hand, it must be very flexible as to provide "effective hinges" in flap, lead-lag, and pitching. The design specifications are particularly severe concerning the torsional stiffness that must be kept extremely low, otherwise the power required by the actuator that control the blade's pitch angle will be unacceptably high.

Filamentary composite materials are a material of choice for such application. In a unidirectional lay-up configuration, the high strength and stiffness fibers will provide the high axial strength required to carry the centrifugal loads and bending moments, and the matrix material will determine to a large extent the torsional behavior of the structure. However, a purely unidirectional lay-up is clearly an unrealistic choice: the transverse and shearing strength of this configuration are very low, and its long-term structural integrity would rely solely on the matrix material. Furthermore, its damage tolerance characteristics are likely to be rather poor. This means that some off-axis fibers will be required, and a three-dimensional fiber architecture such as that obtained by three-dimensional braiding techniques appears to be well-suited for this application, even though the off-axis fibers will increase the torsional stiffness. This "material tailoring" takes advantage of the intrinsic anisotropy of nearly unidirectional composite to attempt meeting the design specifications, however, it is unlikely to be sufficient, rendering "geometric tailoring" a necessity.

Geometric tailoring consists of changes in the flex-structure's cross section. For instance, a rectangular section with a small depth-to-width ratio will present a low flap bending stiffness, forming a virtual flap hinge. However, this section would yield a very high lead-lag bending stiffness. Rotating the section 90 deg would clearly reverse these features. On the other hand, a cruciform-type cross section might have desirable torsional characteristics. It is clear that no one section is likely to possess all the desirable attributes, and the optimal design might involve a number of different cross section and transitional zones.

Finally, the loading environment in which the flex-structure must operate is very severe. The structure must carry very large centrifugal loads, large oscillatory flap bending moments and shear forces due to the time varying aerodynamic lift forces, large oscillatory lead-lag bending moments due to aerodynamic drag forces and flap induced Coriolis forces, and the torsional loads associated with the pitch setting control mechanism and aerodynamic moments. Furthermore, all these forces generate finite displacements and rotations in the flex-structure. These geometric nonlinearities are compounded by the large centrifugal loads which render very significant commonly ignored nonlinearities.

A flex-structure is clearly a very complex component whose intricate dynamic behavior is at the heart of the rotor system. The design and analysis of such a structure is a major challenge that involves the proper modeling of composite materials with highly anisotropic properties, complex geometric configuration, and strongly nonlinear dynamic behavior.

State-of-the-art models for the structural analysis of helicopter blades and flex-structure consist of nonlinear composite beam models.[4] A fundamental assumption underlies many of these models: the cross section of the beam is assumed to be undeformable in its own plane, even though out-of-plane warpings are sometimes allowed. This assumption results in accurate models for helicopter blades that often have closed sections with a core material to prevent any in-plane deformation, however, it is questionable when applied to flex-

---

Received June 12, 1992; revision received Feb. 16, 1994; accepted for publication March 21, 1994.

*Associate Professor, Department of Mechanical Engineering, Aeronautical Engineering, and Mechanics.

†Graduate Assistant, Department of Mechanical Engineering, Aeronautical Engineering, and Mechanics.

structures with an open cross section. The first important deviation from this assumed deformation pattern is the likely presence of chordwise bending: for a thin rectangular section with a nearly unidirectional lay-up, the chordwise bending stiffness is very low and is likely to result in significant chordwise deformation. In the nonlinear regime, these chordwise deformations will affect both bending and torsional behavior and are a source of additional flexibility of the structure. Furthermore, local stress distributions are not likely to be accurately predicted by beam theory. It was shown in Ref. 5 that the geometric stiffening of a beam with an open cross section depends on the distribution of axial stresses, and hence, cannot be accurately predicted by a beam theory involving stress resultants only. It will be shown in this article that the torsional behavior of flex-beams is particularly sensitive to centrifugal stiffening.

In view of this discussion, it is clear that a beam model is inadequate to capture the dynamic behavior of composite flex-structures. Bauchau and Chiang[6] have proposed a nonlinear, anisotropic shell model that accommodates transverse shearing deformations and arbitrary displacements and rotations, but small strains. The finite element is based on a mixed formulation where displacements, internal forces, and momenta are three independent field variables. The mixed formulation alleviates the shear locking phenomena. However, cubic interpolation functions must be used for displacements and rotations of this element to give satisfactory behavior. The resulting model is computationally expensive as it involves the solution for three unknown fields and requires a high order element.

This article will focus on the development of a computationally efficient, displacement-based, nonlinear shallow shell element. This new model has six degrees-of-freedom (DOF) at each node, considerably easing its use in complex structural configurations, as it allows the direct assembly of elements involving finite rotations such as beams and shells, and their intersection at arbitrary angles. Arbitrary large displacements and rotations are allowed, but strains are assumed to remain small. the effect of high anisotropy of the material on both in-plane and bending behaviors of the structure are modeled rationally. The possible presence of elastic coupling is allowed in the model. Transverse shearing deformations are also taken into account as moderately thick structures are to be modeled.

Shell Model

Let r_0 be the position vector of an arbitrary point on the middle surface of the shell, and let ζ be the material coordinate along the normal n, so that the position vector of an arbitrary material point of the shell can be written as (see Fig. 1)

$$r(\xi^1, \xi^2, \zeta) = r_0(\xi^1, \xi^2) + \zeta n(\xi^1, \xi^2) \tag{1}$$

where ξ^1 and ξ^2 are material coordinates used to represent the shell's midsurface.

The coordinates ξ^1, ξ^2, ζ form a set of curvilinear coordinates that are a natural choice of coordinates to describe the shell, and assume that ξ^1 and ξ^2 are chosen to be the lines of curvature. The base vectors[7] of the undeformed shell are

$$g_\alpha = [1 - (\zeta/R_\alpha)]a_\alpha, \qquad g_3 = n \tag{2}$$

where R_α, $\alpha = 1, 2$, are the principal radii-of-curvature.

The metric tensor[7] of the undeformed configuration is $g_{ij} = g_i \cdot g_j$. Note that the base vectors are mutually orthogonal, but are not unit vectors, except for the normal vector g_3. It is convenient to introduce a triad at the shell's midplane

$$e_\alpha = (a_\alpha/\sqrt{a_{\alpha\alpha}}), \qquad e_3 = n \tag{3}$$

where $a_{\alpha\alpha}$ are the first fundamental forms of the surface.

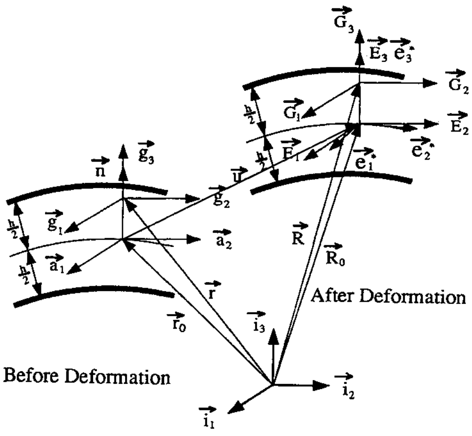

Fig. 1 Geometry of the shell.

The triad e_i can be viewed as a rotation of the base reference triad i_i through a given rotation matrix $t^T(\xi^1, \xi^2)$ such that

$$\underline{e} = t^T \underline{i} \tag{4}$$

Let R be the position vector of an arbitrary material point after deformation. The base vectors in the deformed configuration are

$$G_\alpha = \frac{\partial R}{\partial \xi^\alpha}, \qquad G_3 = \frac{\partial R}{\partial \zeta} \tag{5}$$

and these base vectors at the midplane become

$$E_\alpha = \left.\frac{\partial R}{\partial \xi^\alpha}\right|_{\zeta=0}, \qquad E_3 = \left.\frac{\partial R}{\partial \zeta}\right|_{\zeta=0} \tag{6}$$

The basic assumption used in this work is a material line originally straight and normal to the midplane of the shell does not stretch and remains straight. However, it is not necessarily normal to the deformed midplane of the shell. This assumption departs from the Kirchhoff-Love assumption since it does allow transverse shearing deformations. Based on this assumption, the position vector after deformation can be written as

$$R = R_0 + \zeta E_3 \tag{7}$$

where E_3 is a unit vector, due to the assumed inextensibility of a normal material line.

If the displacement vector of the midplane is denoted u, then

$$R = r_0 + u + \zeta E_3 \tag{8}$$

Due to in-plane straining of the plate, the vectors E_1 and E_2 do not remain unit vectors, nor orthogonal to each other. A triad e_i^* can be defined as follows:

$$\begin{aligned}(E_1/\sqrt{a_{11}}) &= (1 + \bar{e}_{11})e_1^* + \bar{e}_{12}e_2^* + 2\bar{e}_{13}e_3^* \\ (E_2/\sqrt{a_{22}}) &= \bar{e}_{21}e_1^* + (1 + \bar{e}_{22})e_2^* + 2\bar{e}_{23}e_3^* \\ E_3 &= e_3^*\end{aligned} \tag{9}$$

where $\bar{e}_{11}$, $\bar{e}_{22}$, $\bar{e}_{21}$, $\bar{e}_{12}$, $\bar{e}_{13}$, and $\bar{e}_{23}$ are unknown, strain-related parameters. The derivatives of this triad with respect to the material coordinates are

$$\left|\begin{matrix} e_1^* \\ e_2^* \\ e_3^* \end{matrix}\right|_{,\xi^\alpha} = \begin{bmatrix} 0 & K_{3\alpha} & -K_{2\alpha} \\ -K_{3\alpha} & 0 & K_{1\alpha} \\ K_{2\alpha} & -K_{1\alpha} & 0 \end{bmatrix} \left|\begin{matrix} e_1^* \\ e_2^* \\ e_3^* \end{matrix}\right| \tag{10}$$

The base vectors in the deformed configuration are obtained by combining Eq. (5) to Eq. (10), to find

$$
\begin{aligned}
(\boldsymbol{G}_1/\sqrt{a_{11}}) &= (1 + \bar{e}_{11} + \zeta K_{21})\boldsymbol{e}_1^* \\
&\quad + (\bar{e}_{12} - \zeta K_{11})\boldsymbol{e}_2^* + (2\bar{e}_{13})\boldsymbol{e}_3^* \\
(\boldsymbol{G}_2/\sqrt{a_{22}}) &= (\bar{e}_{21} + \zeta K_{22})\boldsymbol{e}_1^* \\
&\quad + (1 + \bar{e}_{22} - \zeta K_{12})\boldsymbol{e}_2^* + (2\bar{e}_{23})\boldsymbol{e}_3^* \\
\boldsymbol{G}_3 &= \boldsymbol{e}_3^*
\end{aligned}
\tag{11}
$$

The metric tensor in the deformed configuration can be readily obtained as $G_{ij} = \boldsymbol{G}_i \cdot \boldsymbol{G}_j$.

The Green-Lagrange strain components f_{ij} are defined as $f_{ij} = \frac{1}{2}(G_{ij} - g_{ij})$. These strains are expressed in the material curvilinear coordinate system defined by the base vector $\boldsymbol{g}_i$. It is more convenient to express these strain components in the locally rectangular coordinate system defined by the midplane base vectors $\boldsymbol{e}_i$ of the undeformed configuration. These two sets of strains are related by[7]:

$$\varepsilon_{ij} = f_{pq} \frac{\partial \alpha^p}{\partial \bar{\alpha}^i} \frac{\partial \alpha^q}{\partial \bar{\alpha}^j} \tag{12}$$

We now focus our attention on shallow shell structure, i.e., initial curvatures $1/R_\alpha$ are assumed to be small compared with unity. Furthermore, the strain-related parameters $\bar{e}_{ij}$, and curvature related strains ζK_{ij} are also assumed to remain small compared with unity, the strain-displacement relationships then become

$$
\begin{aligned}
\varepsilon_{11} &= \bar{e}_{11} + \zeta\kappa_{11}, \quad \kappa_{11} = K_{21} + 1/R_1, \quad \gamma_{13} = 2\bar{e}_{13} \\
\varepsilon_{22} &= \bar{e}_{22} + \zeta\kappa_{22}, \quad \kappa_{22} = K_{12} + 1/R_2, \quad \gamma_{23} = 2\bar{e}_{23} \\
\gamma_{12} &= \bar{e}_{12} + \bar{e}_{21} + \zeta\kappa_{12}, \quad \kappa_{12} = K_{22} - K_{11}
\end{aligned}
\tag{13}
$$

The strain and curvature components must now be related to the displacement components. The midplane displacement vector is resolved in the base triad as

$$\boldsymbol{u} = u_1\boldsymbol{i}_1 + u_2\boldsymbol{i}_2 + u_3\boldsymbol{i}_3 \tag{14}$$

Combining Eqs. (6), (8), and (13) yields:

$$(\boldsymbol{E}_\alpha/\sqrt{a_{\alpha\alpha}}) = [t_{j\alpha} + (u_{j,\alpha}/\sqrt{a_{\alpha\alpha}})]\boldsymbol{i}_j = u_{j\alpha}\boldsymbol{i}_j \tag{15}$$

The triad $\boldsymbol{e}_i^*$ can be viewed as a rotation of the base reference triad $\boldsymbol{i}_i$ through an unknown rotation tensor $T_e(\xi^1, \xi^2)$ such that

$$\underline{e}^* = (T_e t)\underline{i} \tag{16}$$

Identifying the base vectors at the shell's midplane in Eqs. (9) and (15), and with the help of Eq. (16), the strain related parameters are obtained as

$$
\begin{vmatrix} \bar{e}_{11} \\ \bar{e}_{12} \\ 2\bar{e}_{13} \end{vmatrix} = t^T T_e^T \begin{vmatrix} u_{11} \\ u_{21} \\ u_{31} \end{vmatrix} - \begin{vmatrix} 1 \\ 0 \\ 0 \end{vmatrix}, \quad
\begin{vmatrix} \bar{e}_{21} \\ \bar{e}_{22} \\ 2\bar{e}_{23} \end{vmatrix} = t^T T_e^T \begin{vmatrix} u_{12} \\ u_{22} \\ u_{32} \end{vmatrix} - \begin{vmatrix} 0 \\ 1 \\ 0 \end{vmatrix}
\tag{17}
$$

With this formulation an ambiguity remains about the orientation of the $\boldsymbol{e}_i^*$ triad, which can freely rotate about the normal $\boldsymbol{e}_3^*$. To eliminate this ambiguity, the constraint $\bar{e}_{12} = \bar{e}_{21}$ is added to the formulation. This constraint relates the rotation about the normal to the in-plane displacement providing the shell a stiffness with respect to a torsional moment normal to its surface. The model has six kinematic DOF: the three midplane displacement components u_i, and the three finite rotation components that define the finite rotation tensor T_e.

Strain Energy Expression

The strain energy of a shell structure can be written as

$$U = \frac{1}{2}\int_{S_m}\int_h (\underline{\varepsilon}^{kT} Q_e^k \underline{\varepsilon}^k + \underline{\gamma}^{kT} Q_s^k \underline{\gamma}^k)\, \mathrm{d}\zeta\, \mathrm{d}S_m = U_e + U_s \tag{18}$$

where U_s is the shearing strain energy; U_e is membrane and bending strain energy; $\underline{\varepsilon}^k = \lfloor \varepsilon_{11}^k, \varepsilon_{22}^k, \gamma_{12}^k \rfloor^T$, and $\underline{\gamma}^k = \lfloor \gamma_{13}^k, \gamma_{23}^k \rfloor^T$ are the in-plane and out-of-plane strain components both defined in Eq. (13); Q_e^k is the kth ply in-plane stiffness matris; Q_s^k is the kth ply shearing stiffness matrix; S_m is the midplane surface; and h is the thickness of the shell.

U_e is

$$U_e = \frac{1}{2}\int_{S_m}\int_h (\underline{\varepsilon}^{kT} Q_e^k \underline{\varepsilon}^k)\, \mathrm{d}\zeta\, \mathrm{d}S_m = \frac{1}{2}\int_{S_m} \underline{e}_s^{*T} C_e^* \underline{e}_e^*\, \mathrm{d}S_m \tag{19}$$

where $\underline{e}_e^* = \lfloor \bar{e}_{11}\ \bar{e}_{22}\ \bar{e}_{12} + \bar{e}_{21}\ \kappa_{11}\ \kappa_{22}\ \kappa_{12} \rfloor^T$ are the through-the-thickness average in-plane strain components, and C_e^* is the average through-the-thickness membrane and bending stiffness matrix.

U_s is

$$U_s = \frac{1}{2}\int_{S_m}\int_h (\underline{\gamma}^{kT} Q_s^k \underline{\gamma}^k)\, \mathrm{d}\zeta\, \mathrm{d}S_m = \frac{1}{2}\int_{S_m} \underline{e}_s^{*T} C_s^* \underline{e}_s^*\, \mathrm{d}S_m \tag{20}$$

where $\underline{e}_s^* = \lfloor 2\bar{e}_{13}\ 2\bar{e}_{23} \rfloor^T$ are the average shear strain components, and C_s^* is the average through-the-thickness shear stiffness matrix.

Kinetic Energy Expression

Before evaluation of the kinetic energy function, several sets of triad are defined first as shown in Fig. 2. Let the triad $\boldsymbol{I}$ be an inertial reference frame, and the triad $\boldsymbol{i}$ be a frame undergoing rigid body translation $\boldsymbol{P}_r$ and rigid body rotation R with respect to the $\boldsymbol{I}$ frame. The triad $\boldsymbol{e}$ oriented along the material coordinates of the shell structure before deformation is related to the triad $\boldsymbol{i}$ by the initial position vector $\boldsymbol{r}_0$ and a known rotation matrix t. The triad $\boldsymbol{e}$, which is used to describe the material coordinates of a shell structure after deformation, is related to the triad $\boldsymbol{e}$ by an elastic displacement vector $\boldsymbol{u}$ and an unknown rotation matrix T_e.

The position vector $\boldsymbol{P}$, of an arbitrary point of the shell can be written as

$$\boldsymbol{P} = \boldsymbol{P}_r + \boldsymbol{r}_0 + \boldsymbol{u} + \boldsymbol{c} \tag{21}$$

where $\boldsymbol{c}$ is the position vector from the midplane to an arbitrary point of the shell. The components of $\boldsymbol{P}$ in the inertial frame $\boldsymbol{I}$ are

$$
\begin{aligned}
\underline{P}^{[I]} &= \underline{P} = \underline{P}_r^{[I]} + R^{[i]}(r_0^{[i]} + u^{[i]}) \\
&\quad + R^{[I]} T_e^{[i]} t^{[i]} c^{[e^*]} = \underline{P}_r + R(\underline{r}_0 + \underline{u}) + R T_e t \underline{c}
\end{aligned}
\tag{22}
$$

where the notation $(\cdot)^{[\cdot]}$ is used to define the reference frame in which the corresponding tensor components are measured, and $\underline{c} = \underline{c}^{[e^*]} = \lfloor 0\ 0\ \zeta \rfloor^T$.

The inertial velocities are now

$$\dot{\underline{P}}^{[I]} = \dot{\underline{P}}_r^{[I]} + \dot{R}(\underline{r}_0 + \underline{u}) + R\dot{\underline{u}} + (\dot{R}T_e t + \dot{R}T_e t)\underline{c} \tag{23}$$

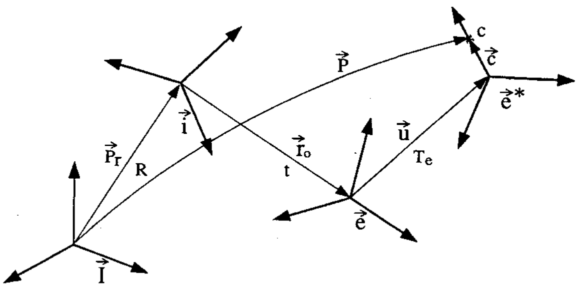

Fig. 2 Coordinate systems.

and expressed in the deformed frame become

$$\underline{\dot{P}}^{[e^*]} = t^T T_e^T R^T \underline{\dot{P}}^{[I]} = \underline{\hat{v}}^* + \tilde{\omega}_t^* \underline{c} \tag{24}$$

where

$$\underline{\hat{v}}^* = t^T T_e^T \underline{\hat{v}} = t^T T_e^T [\underline{\dot{u}} + \tilde{\omega}_r(\underline{r}_0 + \underline{u}) + R^T \underline{\dot{P}}_r] \tag{25}$$

$$\tilde{\omega}_t^* = t^T T_e^T \underline{w}_r + t^T \underline{w}^*$$

and $\underline{w}_r$ are the components of the skew symmetric matrix, $\tilde{w}_r = R^T\dot{R}$; $\underline{w}^*$ are the components of the skew symmetric matrix, $\tilde{w}^* = T_e^T\dot{T}_e$. Finally, the inertial velocity of a material point in the deformed triad $\boldsymbol{e}$ becomes

$$\dot{\boldsymbol{P}} = \lfloor \boldsymbol{e}_1\ \boldsymbol{e}_2\ \boldsymbol{e}_3 \rfloor \begin{vmatrix} \hat{v}_1^* + \omega_{t2}^*\zeta \\ \hat{v}_2^* - \omega_{t1}^*\zeta \\ \hat{v}_3^* \end{vmatrix} \tag{26}$$

The kinetic energy of the system is

$$T = \frac{1}{2}\int_{S_m}\int_h \rho\dot{P}\cdot\dot{\boldsymbol{P}}\, \mathrm{d}\zeta\, \mathrm{d}S_m = \frac{1}{2}\int_{S_m} \underline{v}^{*T} M^* \underline{v}^*\, \mathrm{d}S_m \tag{27}$$

where $\underline{v}^{*T} = \lfloor \underline{\hat{v}}^{*T}, \underline{w}^{*T} \rfloor$ are the velocities

$$M^* = \begin{bmatrix} m & 0 & 0 & 0 & m_3 & 0 \\ 0 & m & 0 & -m_3 & 0 & 0 \\ 0 & 0 & m & 0 & 0 & 0 \\ 0 & -m_3 & 0 & m_{33} & 0 & 0 \\ m_3 & 0 & 0 & 0 & m_{33} & 0 \\ 0 & 0 & 0 & 0 & 0 & m_{00} \end{bmatrix}$$

$$(m, m_3, m_{33}) = \int_h \rho(1, \zeta, \zeta^2)\, \mathrm{d}\zeta \tag{28}$$

and m_{00} is a fictitious moment of inertia corresponding to the in-plane rotation DOF.

In the finite element approximation, nine-noded Lagrangian elements were used. The midplane displacement components u_i, and the three finite rotation parameters defining the finite rotation tensor T_e are all interpolated using quadratic shape functions. In this work the conformal rotation vector is used to parametrize the finite rotations. The constraint $\bar{e}_{12} = \bar{e}_{21}$ is enforced via a penalty formulation.

Validation of the Formulation

The performance of the present shell element was validated by solving several benchmark problems, which include 1) shear locking, 2) cylindrical bending, 3) drilling DOF, 4) shell roof, 5) nonlinear response, and 6) natural frequency. The execution time for the present displacement-based formulation was found to be a factor of 6 faster than the mixed formulation of Ref. 5.

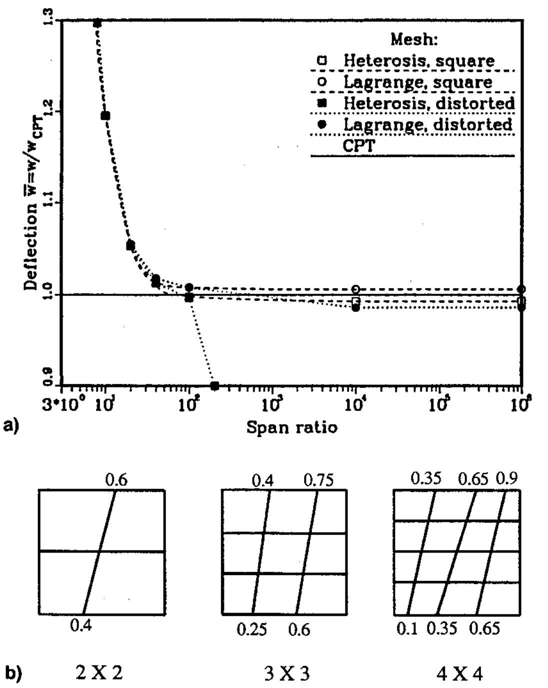

Fig. 3 Shear locking study: a) center deflection of a plate under uniform loading and b) distorted meshes.

Shear Locking

The first benchmark problem deals with the shear locking phenomenon. In order to eliminate shear locking, this shell element employs selective-reduced quadrature, i.e., full integration for evaluating the bending and membrane stiffness terms while one-order less quadrature for calculating shearing stiffness terms and the constraint (this is referenced to as a "Lagrange element"). Although spurious kinematic modes can occur with this formulation, they are suppressed by the clamped boundary condition associated with typical flexstructures. Figure 3a shows the center transverse deflection of a rigidly clamped square plate subjected to a uniformly distributed load vs plate thickness. The excellent correlation with analytical results for even an extremely thin plate (width-to-thickness ratio of 10^6), clearly demonstrate that the present formulation does not lock for both rectangular and distorted meshes (see Fig. 3b). The Heterosis element[8] exhibits the locking phenomena when distorted meshes are used.

Cylindrical Bending

The second benchmark problem deals with the cylindrical bending of a plate for which analytical results[9] are available based on the three-dimensional theory of elasticity. Classical laminated plate theory (CPT) results are also available[10] (CPT is based on the Kirchhoff-Love assumptions, i.e., neglected shearing deflection). The square plate of length L with highly anisotropic material is simply supported along two opposite edges and subjected to a sinusoidally distributed transverse loading $P = P_0 \sin(\pi x/L)$. Two different lay-ups were considered, a [90 deg/0 deg]$_T$ unsymmetrical laminate, and a [0 deg/90 deg/0 deg]$_T$ symmetric laminate.

This problem was treated in Ref. 5, and an excellent correlation is observed between the present results, those of Ref. 5, and the three-dimensional elasticity solution for the midspan deflection, whereas CPT underestimates transverse deflection for a low aspect ratio. Good correlation is found for the stress distribution for large plate width-to-thickness aspect ratios $S \geq 10$, however, when $S = 4$, large discrepancies are observed between the three-dimensional elasticity solution and the present results. This means that both the mixed and the present displacement-based formulations are good at predicting the overall stiffness of the plate (as shown by the good correlation in overall transverse deflection), whereas local

Table 1 Results of slab-to-column connection

	$-u_A = v_A$	$10^3 \times \theta_{ZA}$	$10^3 \times \phi$
Couples of forces	0.07890	0.39450	0.394662
Concentrated moments	0.07894	0.39470	0.394662
Beam theory			0.394662

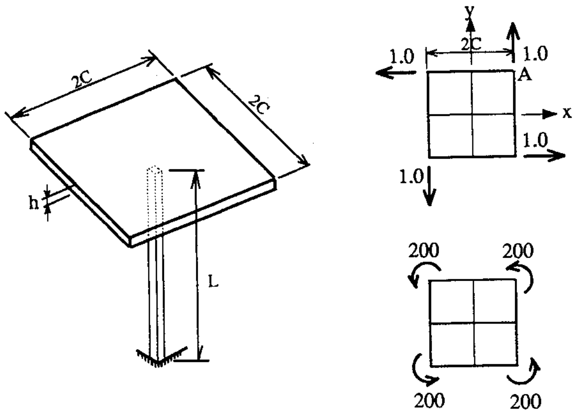

Fig. 4 Slab supported by a central column.

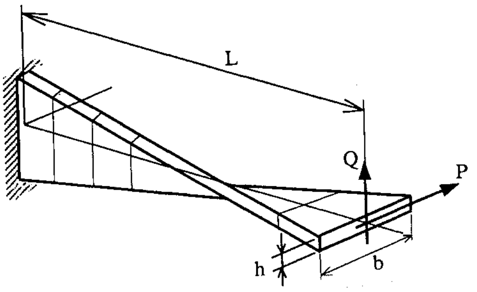

Fig. 5 Twisted plate under tip loads.

stress prediction can be fairly inaccurate for thick plate. This does not seem to be a major limitation of the model because it is intended for the dynamic analysis of rotor flex-structures, and not for local stress predictions.

Sixth DOF

In order to test the performance of the sixth DOF of the shell (i.e., rotation normal to the plane of the shell), two different structural configurations are studied in the third benchmark problem. First, a horizontal square slab is sustained by a vertical central column and loaded by a resultant in-plane moment M_z = 800 lbf, which is applied by four horizontal forces or by four concentrated moments, acting at the corners as shown in Fig. 4. The material properties are Young's modulus $E = 2 \times 10^6$ psi, Poisson's ratio $\nu = 0.3$, the plate thickness $h = 1.0$ in., the width of the slab is $2C = 400$ in., the height of the column is $L = 300$ in., and the column's St. Venant torsional stiffness is 790.55 lb-in.^{2}.

The response of corner A of the slab is shown in Table 1. u_A and v_A are the horizontal displacements of corner A in the x and y directions, respectively, θ_{ZA} is the in-plane rotation of corner A. Since the plate is rather stiff compared to the column, θ_{ZA} also indicates the overall rotation of the slab. The rotation ϕ is the twist value at the connection between the slab and column, measured as the tip rotation of the beam. As observed in Table 1, the present results are good agreement with beam theory, and indicate the correct behavior of the sixth DOF as a means of transferring the loads from the plate to the beam.

Table 2 Tip deflections of a twisted plate

	$Q = 1.0$		$P = 1.0$	
Model	$U2$	$U3$	$U2$	$U3$
Plate 1 × 12	1.7153	1.7479	5.4212	1.7151
Plate 3 × 18	1.7171	1.7499	5.4183	1.7171
Beam 8	1.7187	1.7496	5.4293	1.7187
Analytical		1.750	5.426	

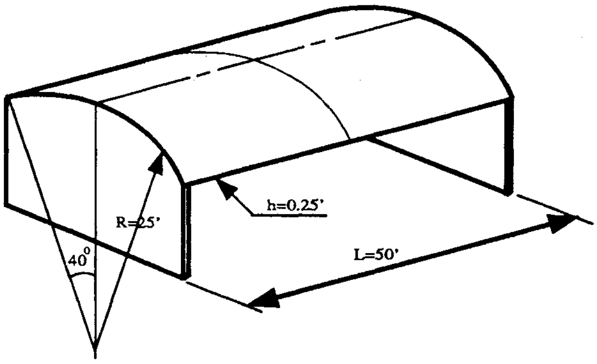

Fig. 6 Scordelis-Lo shallow roof structure.

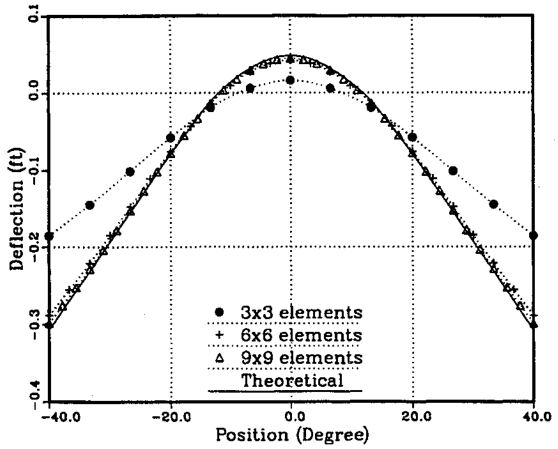

Fig. 7 Midsection vertical deflection of the Scordelis-Lo roof under its own weight.

Next, a cantilever plate of rectangular cross section with span $L = 12$ in., width $b = 1.1$ in.,and thickness $h = 0.32$ in., and a twist of 90 deg over its length, is subjected to a concentrated unit load (either $P = 1$ lb or $Q = 1$ lb) at its free end (Fig. 5). The twisted plate has a small curvature radius-to-thickness ratio, and undergoes large rotation together with bending behavior. For comparison, a beam model with eight cubic elements is used as reference. Table 2 shows the finite element results obtained from both shell and beam models as well as an analytical solution from Frey.[11] The present shell element which has the in-plane rotation DOF predicts the responses of this type structure accurately even when a coarse mesh (1 × 12) is used. Shell models ignoring the sixth DOF were shown[11] to inaccurately predict the response of the structure.

Shell Roof

The fourth benchmark problem is a thin cyindrical shell roof, also known as Scordelis-Lo shallow roof, in which both membrane and bending actions are significant. The particular example originally solved by Scordelis and Lo[12] has been frequently used since for assessing finite element performance,[13,14] and hence, will be used here for comparison purposes. Figure 6 shows the geometrical and physical characteristics of the problem with the Young's modulus $E = 30 \times 10^3$ ksi, Poisson's ratio $\nu = 0.0$. This shell roof is supported at both ends on rigid diaphragms, and under the action of self-weigh ω = 90 lbf/ft^2. The vertical deflections at the midsection are investigated and compared with the existing results as shown in Fig. 7, while the analytical solution is obtained from Ref. 12. One-quarter of the shell is modeled by 3 × 3, 6 × 6, and 9 × 9 elements. A coarse mesh, 3 × 3, gives poor prediction, whereas finer meshes 6 × 6 and 9 × 9 give results in close agreement with the exact solution.

Nonlinear Response

The fifth benchmark problem is intended to test the nonlinear capability of the shell element. The nonlinear response of a square plate with various boundary conditions is compared with an analytical solution.[15] A simply supported isotropic, square plate (length $L = 1.2$ m, Young's modulus E, Poisson's ratio $\nu = 0.316$, and thickness h) is subjected to a uniform transverse pressure P_0. Due to the symmetry of the problem, a quarter of the plate was analyzed with 4 × 4 biquadratic elements. Figure 8a shows the nondimensional transverse displacement $\bar{w} = w/h$ at the center of the plate vs the nondimensional $\bar{P} = P_0L^4/Eh^4$. A good correlation is found between an analytical slution and the present formulation for various aspect ratios (S = 300, 50, 20). Figure 8b shows the corresponding result for a plate eigidly clamped along its four edges. Finally, we turn to a simply supported orthotropic square plate with stiffness moduli $E_L/E_T = 40$, $G_{LT}/E_T = 0.5$, and $\nu_{TL} = \nu_{LT} = 0.25$. Figure 8c shows that the present results are in good agreement with the analytical solution for high values of the aspect ratio, whereas for low aspect ratio the present analysis predicts deflection about 10% larger than the analytical solution. This discrepancy is probably due to the fact that the analytical solution neglected shearing deformation and hence becomes inaccurate at low aspect ratio.

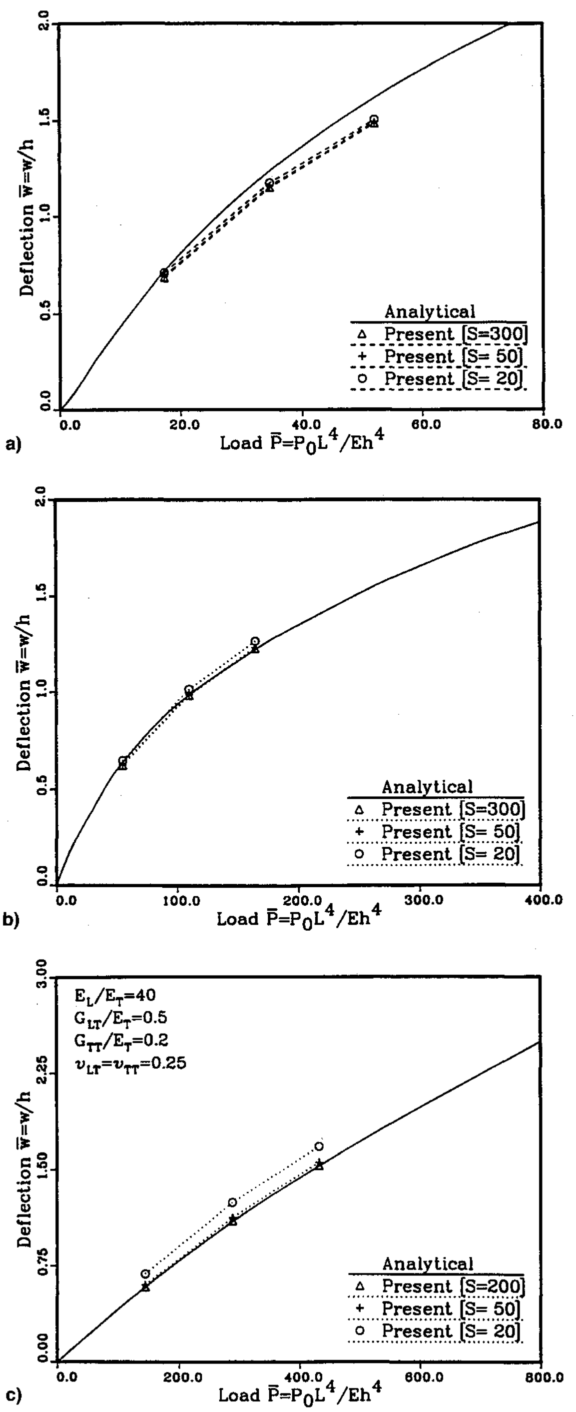

Fig. 8 Center deflection of a plate under uniform load: a) simply supported isotropic plate, b) rigidly clamped isotropic plate, and c) simply supported unidirectional composite plate.

Table 3 Natural frequencies of an anisotropic thick plant (S = 10)

		Exact	Present, 4 × 4		Present, 6 × 6	
m	n	$\bar{\omega}_{mn}$	$\bar{\omega}_{mn}$	Error, %	$\bar{\omega}_{mn}$	Error, %
1	1	4.74	4.729	−0.23	4.733	−0.16
1	2	10.33	10.379	+0.47	10.319	−0.11
2	1	11.88	11.960	+0.67	11.888	−0.06
2	2	16.94	17.056	+0.68	16.955	+0.09
1	3	18.88	19.580	+3.71	19.018	+0.07

Natural Frequency

The last benchmark probem deals with natural vibration frequencies of simply supported, anisotropic square thick plate. An analytical solution[16] obtained from three-dimensional elasticity theory is used for comparison. The following nondimensional natural frequency form is used:

$$\bar{\omega}_{mn} = \omega_{mn}(L^2/h)\sqrt{(\rho/c_{11})}, \qquad m, n = 1, 2, 3, \ldots \tag{29}$$

where c_{11} is the elastic constant such that $\sigma_i = c_{ij}e_j$; i, j = 1–6 with σ_i and e_j are components of the stress and strain.

A set of values with span $L = 1.2$ m, the thickness $h = 0.12$ m such that span-to-thickness ratio $S = 10$, and the material properties:

$$E_1 = 143.62 \text{ GPa}, \quad E_2 = 74.40 \text{ GPa}, \quad G_{12} = 42.05 \text{ GPa}$$
$$G_{13} = 25.58 \text{ GPa}, \quad G_{23} = 47.57 \text{ GPa}, \quad \nu_{12} = 0.44 \tag{30}$$
$$\rho = 1800 \text{ kg/m}^3, \quad c_{11} = 159.94 \text{ GPa}$$

are used. Table 3 lists the present results which are in good agreement with the analytical solution of Ref. 16, labeled "Exact."

Practical Application

We now turn to a practical application for the bearingless helicopter rotor blade problem. The Messerschmitt-Bölkow-Blohm GmbH (MBB) bearingless tail rotor used in the BK117 helicopter is simulated.[17] The flex-structure uses a fiber composite bending-torsion flexure to accommodate flapping and lead-lag deflections, as well as pitch control. Both shell elements and beam elements are employed to model this flex-structure, and their results are compared.

The design of the MBB bearingless four-bladed tail rotor system[17] consists of two double units, with centrifugal loads of opposing blades being carried directly within the fiberglass flex-structure. A flat, rectangular plate attached to the hub presents low flap stiffness, forming the "flapping hinge," whereas a cruciform cross-sectional structure lies between the outboard of the flat plate and the inboard of the blade, providing the functions of "lead-lag hinge" and "pitch bearing."

The MBB rotor is 1.95 m in diam, with a rotation speed of 211.8 rad/s. The flap stiffness, lead-lag stiffness, and mass distribution along the span can be found in Ref. 17. The torsional stiffness was measured to be 0.33 Nm/deg when there

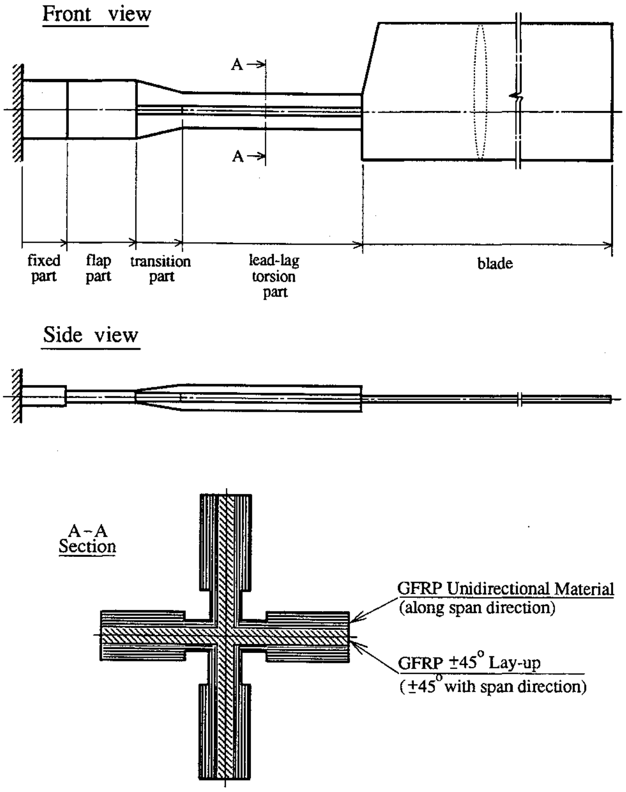

Fig. 9 Geometry of the MBB tail rotor blade.

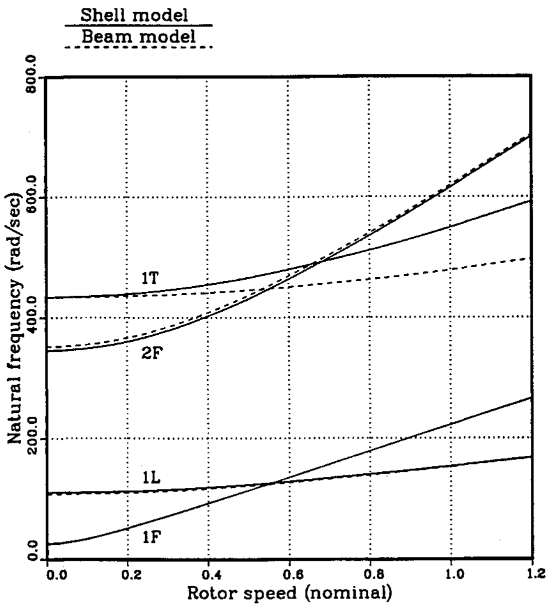

Fig. 10 Southwell plot of the MBB tail rotor.

is no centrifugal force; at the nominal rotor speed, the torsional stiffness was found to increase to 0.5 Nm/deg, based on natural torsional frequency measurements. The fundamental frequencies are 26.0 rad/s in flap direction, and 110.0 rad/s in chordwise direction when the rotor is static, and that fundamental frequencies are 1.043/rev in flap direction, and 0.685/rev in chordwise direction when the rotor is at the nominal speed condition. Figure 9 shows a sketch of a single rotor blade. Since the stability analysis of this system is beyond the scope of this research, the damping materials mounted on the cruciform structure to provide the lead-lag damping in the original design of MBB will not be included in this simulation.

The MBB rotor is investigated with two models: 1) shell and 2) beam models. In the shell model, the flex-structure that consists of the fixed, flap, transition, and lead-lag-torsion parts is modeled by shell elements, whereas the blade is modeled by beam elements.[18] A total of 42 9-noded Lagrangian shell elements were used to model the flex-structure, whereas 6 4-noded beam elements were used to model the blade. The warping displacement is assumed to be free at the flex-structure-blade interface. The beam elements used in this effort are described in Ref. 18; they handle arbitrarily large displacements and rotations of naturally curved and twisted an-

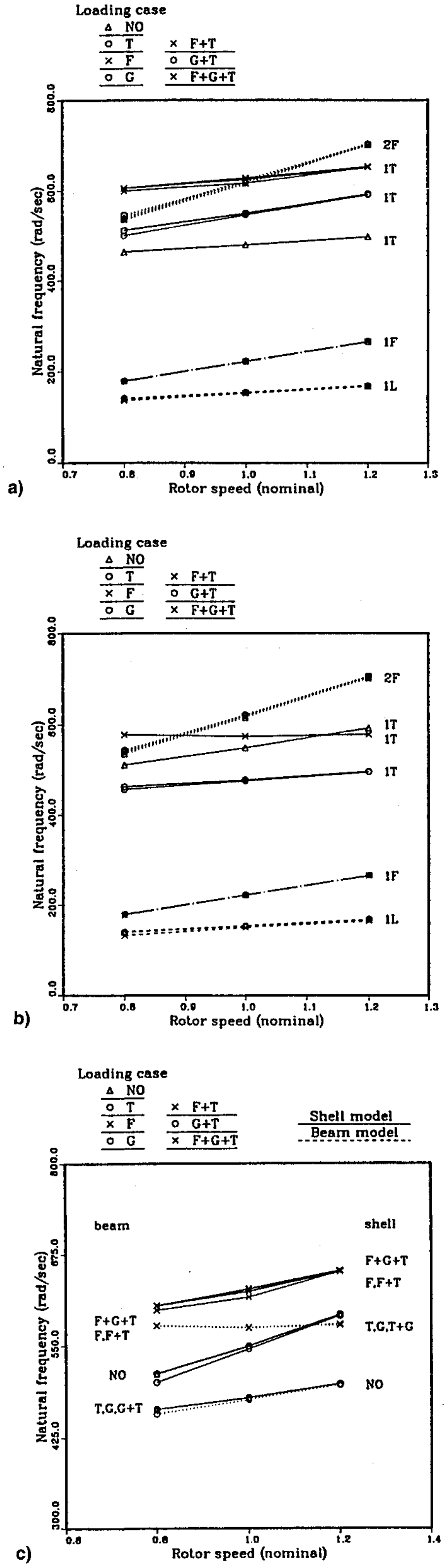

Fig. 11 Southwell plots for the MBB tail rotor under various loading conditions: a) shell model, b) beam model, and c) torsion modes.

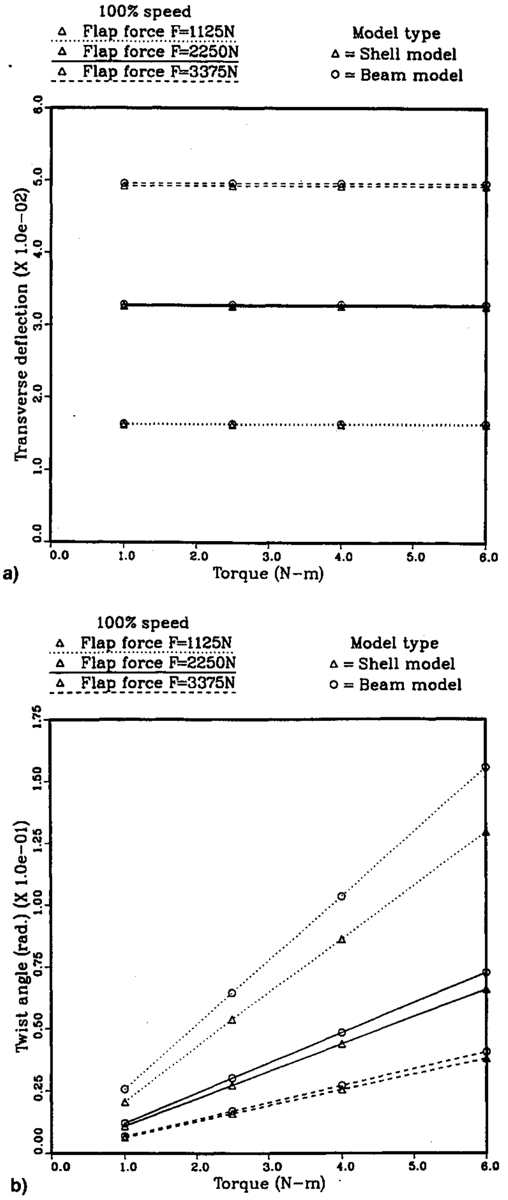

Fig. 12 Deflections at the junction under flap and torque loads: a) out-of-plane deflections and b) twist angle.

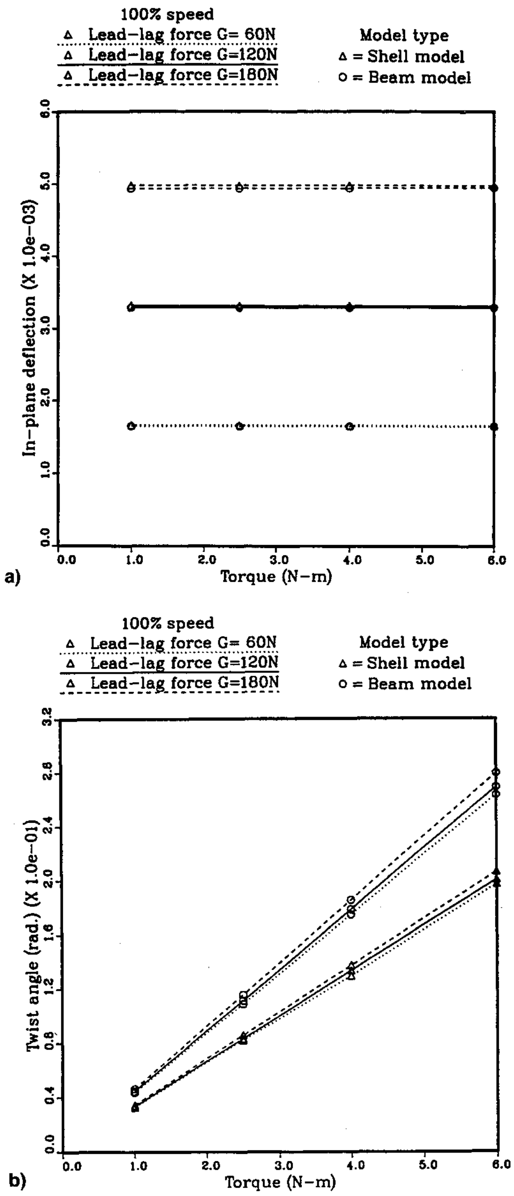

Fig. 13 Deflections at the junction under lead-lag and torsion loads: a) in-plane deflection and b) twist angle.

isotropic beams including transverse and warping deformations effects. The six degrees-of-freedom capability of the shell element is very convenient to model the cruciform components where shell elements intersect at a 90-deg angle. In the beam model, the whole rotor system, i.e., both flex-structure and blade, are modeled using 10 4-noded beam elements. Both models have the same static (i.e., flap, lead-lag, torsion, and axial stiffnesses) and dynamic (i.e., mass distribution, natural frequencies in flap, lead-lag, and torsion) characteristics when the rotor blade is in a nonrotating condition, and these characteristics match that of the MBB rotor system.

Figure 10 shows the Southwell plots for both models. Little difference in flapping and lead-lag natural frequencies is observed between the two models, whereas a significant discrepancy in the torsion natural frequency between the shell and beam models is apparent. This is consistent with the fact that the geometric stiffness of a beam with an open section depends on the distribution of axial stresses,[5] and hence, cannot be accurately predicted by a beam theory involving stress resultant only. The shell model provides a better resolution of the cross-sectional deformations, and hence, a more accurate representation of this geometric stiffening effect.

Next, the natural frequency of the rotor blade subjected to specific applied loads is investigated. These applied loads include a flapping load $F = 1125$ N acting at the blade tip, a lead-lag load $G = 60$ N acting at the tip also, and a torque $T = 1$ Nm acting at the junction between the flex-structure and the blade, such that the resulting rotations at this junction are out-of-plane slope $A_2 = 4.5$ deg, in-plane slope $A_3 = 0.8$ deg, and twist $A_1 = 1.9$ deg, respectively, when the rotor is at nominal rotation speed and these loads are imposed individually. The relationship between natural frequencies and applied loads is shown in Figs. 11a and 11b for shell and beam models, respectively. The symbol in the legend of the figure refer to the rotor blade loading condition, for example, $F + G + T$ refers to the flapping load F, lead-lag load G, and torque T being applied simultaneously. As observed from these two figures, the first and second flapping and the first lead-lag natural frequencies are little affected by the applied loads, although the first torsion natural frequency is strongly affected by the loading type. Figure 11c focuses on the fundamental torsion natural frequency under various applied loads for both shell and beam models. The nature of the model and the loading condition significantly affect the torsional frequency.

Next, the deflections of the rotor blade subjected to a flapping load at the blade tip together with a torque at the junction are investigated using the shell and beam models. Figure 12a

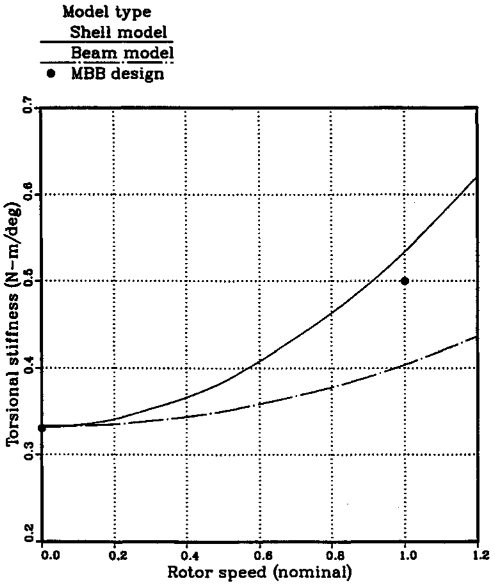

Fig. 14 Torsional stiffness of the flex-structure for the beam and shell models.

shows the tip transverse deflection of the rotor blade at nominal speed. Little difference is observed between the shell and beam models. This contrasts with Fig. 12b, which shows significant discrepancies in the junction twist angle for the shell and beam models.

The same phenomenon is observed when the rotor blade subjected to a lead-lag load at the tip together with a torque at the junction. Figure 13a shows the tip in-plane deflections at nominal speed. Once again, little difference is observed between the two models. However, the junction twist angle shown in Fig. 13b is strongly affected by the model type.

Finally, the behavior of the torsional stiffness for the flex-structure is investigated. In the nonrotating condition, both shell and beam models have the same torsional stiffness of 0.33 Nm/deg for the flex-structure. When the blade is at nominal rotation speed, the torsional stiffness evaluated by the beam model is 0.40 Nm/deg, as shown in Fig. 14, while the shell model is 0.53 Nm/deg, which is in close agreement with the value of 0.50 Nm/deg reported in Ref. 17.

This study has uncovered significant differences in the torsional behavior of the flex-structure of a bearingless rotor in both static and dynamic cases when shell and beam models are used. Torsional frequencies differ for the two models, and are also differently affected by applied loads. Figure 11c shows that this torsional frequency can vary from 457 to 654 rad/s, depending on the model type and applied loading. The shell model can evaluate the torsional characteristics more accurately than the beam model when comparing their predictions with the data reported by MBB.[17]

Conclusions

In this article a nonlinear, anisotropic shallow shell formulation was developed to model helicopter rotor flex-structure. This model includes the effect of transverse shearing deformation, it can rationally handle highly anisotropic laminated composite material and deal with arbitrarily large displacements and rotations, although strains are assumed to remain small. The model is computationally efficient and was validated by comparing its predictions with those of various analytical solutions for linear and nonlinear static deflections, as well as natural vibration frequencies of both isotropic and highly anisotropic materials. Excellent correlation was found for overall deflections and local stresses, however, discrepancies were observed for local stresses when the plates become thick. Hence, this model should be adequate for predicting the overall dynamic behavior of flex-structure. Application of this shell model to a typical flex-structure revealed that the structural dynamic behavior of flex-structure is affected by shell-like deformation modes. This is particularly significant for the torsion mode of the flex-structure. Systematic analytical and experimental investigations into the dynamic behavior of composite flex-structures should be undertaken to improve our understanding of the dynamic behavior of this complex component which is at the heart of bearingless rotor behavior.

Acknowledgment

W. Chiang acknowledges the support of Chung-Shan Institute of Science and Technology, Taiwan, Republic of China, for his studies at the Rensselaer Polytechnic Institute.

References

[1] Johnson, W., *Helicopter Theory*, Princeton Univ. Press, Princeton, NJ, 1980.

[2] Prouty, R. W., *Helicopter Performance, Stability and Control*, PWS Publishers, Boston, MA, 1986.

[3] Bielawa, R. L., "Aeroelastic Characteristics of Composite Bearingless Rotor Blades," *Journal of the American Helicopter Society*, Vol. 22, Oct. 1977, pp. 2–9.

[4] Hodges, D. H., "A Review of Composite Rotor Blade Modeling," *AIAA Journal*, Vol. 28, No. 3, 1990, pp. 551–565.

[5] Borri, M., and Merlini, T., "A Large Displacement Formulation for Anisotropic Beam Analysis," *Meccanica*, Vol. 21, Jan. 1986, pp. 30–37.

[6] Bauchau, O. A., and Chiang, W., "Dynamic Analysis of Rotor Flexbeams Based on Nonlinear Anisotropic Shell Models," *Journal of the American Helicopter Society*, Vol. 38, No. 1, 1993, pp. 55–61.

[7] Washizu, K., *Variational Methods in Elasticity & Plasticity*, 3rd ed., Pergamon, New York, 1982.

[8] Huges, T. J. R., and Cohen, M., "The Heterosis Finite Element for Plate Bending," *Computers and Structures*, Vol. 9, No. 3, 1977, pp. 445–450.

[9] Pagano, N. J., "Exact Solution for Composite Laminates in Cylindrical Bending," *Journal of Composite Material*, Vol. 3, July 1969, pp. 398–411.

[10] Reissner, E., and Stavsky, Y., "Bending and Stretching of Certain Types of Heterogenous Aeolotropic Elastic Plates," *Journal of Applied Mechanics*, Vol. 28, No. 2, 1961, pp. 402–408.

[11] Frey, F., "Shell Finite Elements with Six Degrees-of-Freedom per Node," *Proceedings of the Winter Annual Meeting of the American Society of Mechanical Engineers*, Vol. 3 (San Francisco, CA), 1989, pp. 209–252.

[12] Scordelis, A. C., and Lo, K. S., "Computer Analysis of Cylindrical Shells," *Journal of the American Concrete Institute*, Vol. 61, No. 2, 1964, pp. 539–561.

[13] Ahmad, S., Irons, B. M., and Zienkiewicz, O. C., "Analysis of Thick and Thin Shell Structures by Curved Finite Element," *International Journal for Numerical Methods in Engineering*, Vol. 2, No. 3, 1970, pp. 419–451.

[14] Zienkiewicz, O. C., Taylor, R. L., and Too, J. M., "Reduced Integration Technique in General Analysis of Plates and Shells," *International Journal for Numerical Methods in Engineering*, Vol. 3, No. 2, 1971, pp. 275–290.

[15] Chia, C. Y., *Nonlinear Analysis of Plates*, McGraw-Hill, New York, 1980.

[16] Reddy, J. N., *Energy and Variational Methods in Applied Mechanics*, Wiley, New York, 1984.

[17] Huber, H., Frommlet, H., and Buchs, W., "Development of a Bearingless Helicopter Tail Rotor," *Vertica*, Vol. 5, No. 2, 1981, pp. 131–147.

[18] Bauchau, O. A., and Hong, C. H., "Large Displacement Analysis of Naturally Curved and Twisted Composite Element," *AIAA Journal*, Vol. 25, No. 4, 1987, pp. 1469–1475.